Aerospace Science and Technology 119 (2021) 107085

Contents lists available at ScienceDirect

Aerospace Science and Technology

www.elsevier.com/locate/aescte

Comparative dynamic flight stability of insect-inspired flapping-wing micro air vehicles in hover: Longitudinal and lateral motions

Khanh Nguyen [a], Loan Thi Kim Au [b], Hoang-Vu Phan [a,c], Hoon Cheol Park [a,*]

[a] Department of Smart Vehicle Engineering, Konkuk University, Seoul 05029, South Korea
[b] Department of Aerospace Engineering, Sejong University, Seoul 05006, South Korea
[c] School of Engineering, Swiss Federal Institute of Technology Lausanne (EPFL), Lausanne, Switzerland

ARTICLE INFO

Article history:
Received 8 June 2021
Received in revised form 22 July 2021
Accepted 30 August 2021
Available online 9 September 2021
Communicated by Huihe Qiu

Keywords:
Longitudinal and lateral motions
Stability
Flapping-wing micro air vehicle
Computational fluid dynamics

ABSTRACT

In this paper, we compare the characteristics of hovering stability for two insect-inspired flapping-wing micro air vehicles (FW-MAVs) with different strategies to generate control moments for the longitudinal and lateral attitude controls. The two robots were named according to their control mechanisms, *i.e.*, the Stroke-Plane-Change (SPC), and the Trailing-Edge-Change (TEC). The forces and moments produced by flapping wings were computed by the computational fluid dynamics (CFD) method. The longitudinal and lateral flight characteristics were identified as one fast subsidence mode, one slow subsidence mode, and one divergence oscillation mode. The results revealed that the fast and slow subsidence modes in the longitudinal and lateral motions of the SPC were stabilized faster than those of the TEC, while both of the lateral and longitudinal divergence modes of the SPC were more unstable than those of the TEC. Moreover, the effect of the longitudinal and lateral derivatives on the system poles of the SPC were investigated. The results showed that the major source of instability in the longitudinal motion was the pitching derivative with respect to the horizontal speed, M_u^+. Meanwhile, that in the lateral motion was the rolling derivative with respect to the horizontal side speed, L_v^+. Overall, the time response of the SPC, when the body was disturbed by an external force, was relatively faster than that of the TEC. Therefore, using the SPC mechanism can give the FW-MAV more agility to operate in highly cluttered spaces with obstacles.

1. Introduction

For many centuries, the flight of insects has drawn research attention due to its potential application to insect-inspired flapping-wing micro air vehicles (FW-MAVs) [1,2]. Many works cover wide research areas of the aerodynamics of flapping-wing insects [3–5] and insect-like robots [6–12]. On the other hand, the dynamic stability and flight control of insects have been extensively studied [13–19]. Unlike the bird, the lack of control surfaces at the insect tail causes instability during flight. Essentially, the flapping-wing insect produces forces and control moments by adjusting its wing kinematics or changing its center of gravity (CG) location [20–22]. It is obvious that understanding the stability characteristics of insects plays an extremely important role in the development of hover-capable FW-MAVs. Taylor et al. [17] provided a formal analysis of dynamic stability in a flying insect, which was based on the standard linearized equations of motion (EoM) applied in aircraft dynamic analysis [13]. This framework was then widely used in the flight dynamics for flying insects [13,15,23], and has recently been applied in the analysis of flapping-wing robotic systems [24–26]. In these studies, the rigid body assumption was used to simplify the analyses, in which the body had only six degrees of freedom: three in rotational motion, and three in translational motion. The effect of wing motion on the body was represented by the cycle-average forces and moments over a flapping cycle. Furthermore, since the wing mass was relatively small (less than 5% the total body mass), the gyroscopic inertial terms were neglected. On the other hand, the small disturbance theory from the equilibrium was employed to linearize the EoM [15,24,25,27–29]. As a result, the longitudinal and lateral disturbance motions could be separated independently.

To evaluate the stability of flapping-wing robots, the linearized EoM is determined by the cycle-average stability derivatives and the system parameters. The techniques of eigenvalue and eigenvector are employed to obtain the initial solutions and the time-varying responses

* Corresponding author.
E-mail address: hcpark@konkuk.ac.kr (H.C. Park).

https://doi.org/10.1016/j.ast.2021.107085
1270-9638/

of the system. Based on that, the study can indicate whether the system is stable or not. If unstable, the state variables can be found that cause the instability. In order to determine the EoM, the cycle-average forces and moments were obtained by various approaches for insects [15–17,23,27,30,31] and FW-MAVs [24,25,32]. Taylor et al. [17] conducted an experiment to investigate the longitudinal stability analysis of the desert locust *Schistocerca gregaria*. The authors assumed that the angle of attack of a wing-section was unaffected by the pitch disturbances. This means that all the pitch-rate derivatives were assumed to be zero, which might considerably affect the accuracy of result. Karásek [27] provided a quasi-steady aerodynamic model to investigate the stability of a robotic hummingbird. However, only the translational force was considered in his research, while the components due to rotations were not accounted for in the lateral motion. Au et al. [7] compared the forces generated by flapping wings using unsteady blade element theory (UBET) [33] and computational fluid dynamics (CFD). The cycle-average vertical force estimated by the UBET was about 10% lower than that by the CFD. However, the difference in drag was more than 20%. The reason was that the UBET did not cover the effect of the clap-and-fling mechanism, which serves as a lift-enhancing mechanism, occurring at the outboard area when the two wings approach each other during the stroke reversals [8]. Overall, due to these limitations, these methods are not widely used in the stability analysis for flapping wings. Thus, the CFD method is one of the most trustful options to estimate the stability derivatives of flapping wings. This method allows accurate computation of the derivatives, some of which were underestimated by the other approaches, but when they were compared to the measured ones, accuracy of the estimated forces and moments was still guaranteed [23–25,34,35].

In the recent research of our group [8,24,25,36–39,41], we have been developing FW-MAVs, called KUBeetle, that actually fly, using different strategies to produce control moments. In this work, the two different KUBeetles considered are called the Trailing-Edge-Change (TEC) and the Stroke-Plane-Change (SPC) (Fig. 1). Here, we briefly explain how the two moment generators work. For the TEC [36], the wing kinematics are adjusted by a change of the two wing-root spars, which rotate in the same direction on the longitudinal plane of symmetry to generate the pitch moment, and on the lateral plane of symmetry to produce the roll moment. Meanwhile, the wing-root spars rotate in the opposite directions on the longitudinal symmetry plane to create the yaw moment. For the SPC [38,39], the wing stroke plane can be independently tilted in the longitudinal direction to produce the pitch moment, and the stroke plane is laterally tilted to generate roll moment. Meanwhile, the yaw moment is generated by the trailing edge shift mechanism. These two FW-MAVs were designed to produce sufficient vertical force to compensate for their body weight. The total body mass of the TEC is about 20 g, and it has the wing-beat frequency of 30 Hz [24,25]. Meanwhile, the mass of the SPC is 17.7 g, and its flapping frequency is about 23 Hz [39].

In this study, the hovering longitudinal and lateral stability derivatives of the SPC are presented using the CFD method. Based on the cycle-average stability derivatives, the characteristics of hovering stability of the SPC and TEC are compared with each other. In addition, the influence of each of the derivatives on the stability of the SPC is also studied. The system responses of the SPC and TEC are then compared in each mode of motion.

The paper is organized as follows. Section 2 briefly presents materials and methods including parameters of two flapping-wing robots, EoM, measurement of the wing kinematics, and CFD modeling. In Section 3, we discuss the results of the full longitudinal and lateral stability derivatives of the two FW-MAVs, solutions of EoM, effects of each of the stability derivatives on the solutions of EoM, and time responses of the two systems. Finally, conclusions are made in Section 4.

2. Materials and methods

2.1. Equation of motion

To describe the motion of a flapping wing, the definition of the coordinate system is the same as that in previous works [8,24,25,41]. The fixed coordinate system on the earth is the $O_e x_e y_e z_e$. Meanwhile, the coordinate system, $O_b x_b y_b z_b$ is attached to the body frame to describe the wing motion (Fig. 1), where $O_b x_b z_b$ is the longitudinal plane of symmetry, and $O_b y_b z_b$ is the lateral plane of symmetry. The x_b axis points backward, y_b axis points to the right, and the z_b axis directs upwards, being aligned with the body axis. The reference position of the pivot point located at the origin O is referred to determine the center of gravity (CG) point that is located on the vertical symmetry plane. In this work, the CG of the SPC is measured at 75% of the mean chord, c_{mean} below the stroke plane ($0.75c_{mean}$), while that of the TEC is at $0.6c_{mean}$ below the stroke plane. The CG locations of the two FW-MAVs are slightly different due to the difference in the principles of control moment generation and servo locations. Since a FW-MAV becomes unstable even by rate feedback control when the CG is located above the leading edge of wing [24], and we try to place the CG below the leading edge for stable controlled flight.

Since the rigid body approximation was assumed, the disturbed motion of the FW-MAV could be handled separately: three in the longitudinal motion, and three in the lateral motion. The characteristics of the motion are defined by the longitudinal variables $[u,\ w,\ q,\ \theta]^T$, and the lateral variables $[v,\ p,\ r,\ \phi]^T$, as shown in Fig. 1. The time-dependent EoMs are expressed in Eqs. (1) and (2) for the two modes of motion:

$$\text{Longitudinal EoM:}\quad \begin{bmatrix} \delta\dot{u} \\ \delta\dot{w} \\ \delta\dot{q} \\ \delta\dot{\theta} \end{bmatrix} = \begin{bmatrix} \frac{X_u}{m} & \frac{X_w}{m} & \frac{X_q}{m} & g \\ \frac{Z_u}{m} & \frac{Z_w}{m} & \frac{Z_q}{m} & 0 \\ \frac{M_u}{I_{yy}} & \frac{M_w}{I_{yy}} & \frac{M_q}{I_{yy}} & 0 \\ 0 & 0 & 1 & 0 \end{bmatrix} \begin{bmatrix} \delta u \\ \delta w \\ \delta q \\ \delta\theta \end{bmatrix}, \tag{1}$$

$$\text{Lateral EoM:}\quad \begin{bmatrix} \delta\dot{v} \\ \delta\dot{p} \\ \delta\dot{r} \\ \delta\dot{\phi} \end{bmatrix} = \begin{bmatrix} \frac{Y_v}{m} & \frac{Y_p}{m} & \frac{Y_r}{m} & -g \\ \frac{L_v I_z + N_v I_{xz}}{I_x I_z - I_{xz}^2} & \frac{L_p I_z + N_p I_{xz}}{I_x I_z - I_{xz}^2} & \frac{L_r I_z + N_r I_{xz}}{I_x I_z - I_{xz}^2} & 0 \\ \frac{L_v I_{xz} + N_v I_x}{I_x I_z - I_{xz}^2} & \frac{L_p I_{xz} + N_p I_x}{I_x I_z - I_{xz}^2} & \frac{L_r I_{xz} + N_r I_x}{I_x I_z - I_{xz}^2} & 0 \\ 0 & 1 & 0 & 0 \end{bmatrix} \begin{bmatrix} \delta v \\ \delta p \\ \delta r \\ \delta\phi \end{bmatrix}, \tag{2}$$

where the symbol "δ" indicates small disturbance quantity. The X, Y, and Z stand for the aerodynamic forces in the x_b, y_b, and z_b axes, respectively. The L, M, and N denote the roll, pitch, and yaw moments about the CG point, respectively. Sets of (X_u, X_w, X_q), (Y_v,

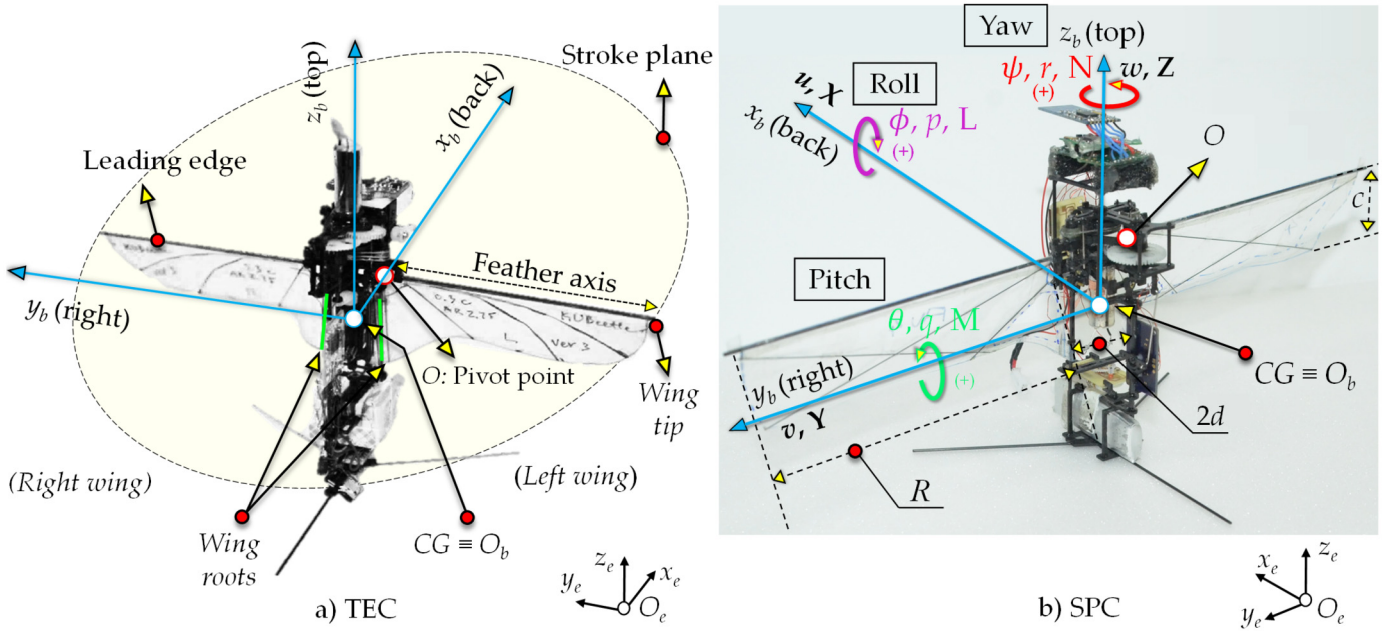

Fig. 1. Definition of the coordinate system of a) the TEC [24,25], and b) the SPC [39], with the state variables: translational velocities (u, v, w), angular velocities (p, q, r), moments about CG (L, M, N), and body attitudes (ϕ, θ, ψ).

Table 1
Morphological parameters of the TEC [24,25] and SPC [39].

	Symbol(s)	TEC	SPC	Unit
Wingbeat amplitude	Φ	190	190	degree
Distance from the pivot point to the symmetry plane	d	8	9.5	mm
Body mass	m	20.0	17.7	g
Flapping frequency	f	30	23	Hz
Mean flapping velocity	U_m	7.26	6.46	ms^{-1}
Disturbance velocity	Δu	0.542	0.453	ms^{-1}
Two-wing area	S	3.41×10^{-3}	3.76×10^{-3}	m^2
Wing length	R	0.069	0.075	m
Mean chord length	c_{mean}	0.025	0.025	m
CG position	z_{cg}	$-0.6c_{mean}$	$-0.75c_{mean}$	
Moments of inertia about the x_b-axis	I_{xx}	2.19×10^{-5}	8.70×10^{-6}	$kg\,m^2$
Moments of inertia about the y_b-axis	I_{yy}	2.17×10^{-5}	7.94×10^{-6}	$kg\,m^2$
Moments of inertia about the z_b-axis	I_{zz}	2.63×10^{-6}	2.38×10^{-6}	$kg\,m^2$
Product of inertia for the zx plane	$I_{xz} = I_{zx}$	-1.68×10^{-8}	-3.94×10^{-7}	$kg\,m^2$

Y_p, Y_r), (Z_u, Z_w, Z_q), (M_u, M_w, M_q), (L_v, L_p, L_r), and (N_v, N_p, N_r) are the dimensional stability derivatives. These terms describe the front-and-backward horizontal force (X), the sideward horizontal force (Y), the vertical force (Z), the roll moment (L), the pitch moment (M), and the yaw moment (N), with respect to the deviations, such as the translational speed variables (u, v, w), and the rotational rate variables (p, q, r). The rotational angles (θ, ϕ, ψ) represent the pitch, roll, and yaw angles, respectively. m is the body mass, and g is the acceleration of gravity. I_{xx}, I_{yy}, and I_{zz} represent the moment of inertia about the x_b, y_b, and z_b axes, respectively. I_{xz} is the product of inertia for the x-z plane. Table 1 compares parameters of the TEC and SPC. The parameters in Table 1 were used for preliminary designs of the final fight models in [24,25] for the TEC and in [39] for the SPC.

The non-dimensional forms of Eqs. (1) and (2) are expressed as below:

$$\text{Longitudinal EoM:} \quad \delta\dot{x}_{\text{long.}}(t) = \mathrm{A}_{long}\delta x_{long.}(t), \tag{3}$$

$$\text{Lateral EoM:} \quad \delta\dot{x}_{\text{lat.}}(t) = \mathrm{A}_{lat}\delta x_{lat.}(t), \tag{4}$$

where $\delta x_{long.}(t)$ and $\delta x_{lat.}(t)$ are the non-dimensional state variable vectors representing the longitudinal variables $[\delta u^+ \ \delta w^+ \ \delta q^+ \ \delta\theta]^T$ and the lateral variables $[\delta v^+ \ \delta p^+ \ \delta r^+ \ \delta\phi]^T$, respectively. A_{long} and A_{lat} are the non-dimensional longitudinal and lateral system matrices, respectively, which are filled by their stability derivatives and system parameters in Eqs. (5) and (6). Note that in Eqs. (5) to (14), the superscript "+" denotes the non-dimensional form of quantities. That is:

$$\text{Longitudinal system matrix:} \quad \mathrm{A}_{long} = \begin{bmatrix} \frac{X_u^+}{m^+} & \frac{X_w^+}{m^+} & \frac{X_q^+}{m^+} & g^+ \\ \frac{Z_u^+}{m^+} & \frac{Z_w^+}{m^+} & \frac{Z_q^+}{m^+} & 0 \\ \frac{M_u^+}{I_y^+} & \frac{M_w^+}{I_y^+} & \frac{M_q^+}{I_y^+} & 0 \\ 0 & 0 & 1 & 0 \end{bmatrix} \tag{5}$$

Lateral system matrix:
$$A_{lat} = \begin{bmatrix} \frac{Y_v^+}{m^+} & \frac{Y_p^+}{m^+} & \frac{Y_r^+}{m^+} & -g^+ \\ \frac{L_v^+ I_z^+ + N_v^+ I_{xz}^+}{I_x^+ I_z^+ - I_{xz}^{+2}} & \frac{L_p^+ I_z^+ + N_p^+ I_{xz}^+}{I_x^+ I_z^+ - I_{xz}^{+2}} & \frac{L_r^+ I_z^+ + N_r^+ I_{xz}^+}{I_x^+ I_z^+ - I_{xz}^{+2}} & 0 \\ \frac{L_v^+ I_{xz}^+ + N_v^+ I_x^+}{I_x^+ I_z^+ - I_{xz}^{+2}} & \frac{L_p^+ I_{xz}^+ + N_p^+ I_x^+}{I_x^+ I_z^+ - I_{xz}^{+2}} & \frac{L_r^+ I_{xz}^+ + N_r^+ I_x^+}{I_x^+ I_z^+ - I_{xz}^{+2}} & 0 \\ 0 & 1 & 0 & 0 \end{bmatrix} \quad (6)$$

Forces:
$$X^+ = \frac{X}{0.5\rho U_m^2 S}, \quad Y^+ = \frac{Y}{0.5\rho U_m^2 S}, \quad Z^+ = \frac{Z}{0.5\rho U_m^2 S} \quad (7)$$

Moments:
$$L^+ = \frac{L}{0.5\rho U_m^2 Sc}, \quad M^+ = \frac{M}{0.5\rho U_m^2 Sc}, \quad N^+ = \frac{N}{0.5\rho U_m^2 Sc} \quad (8)$$

Translational speed variables:
$$u^+ = \frac{u}{U_m}, \quad v^+ = \frac{v}{U_m}, \quad w^+ = \frac{w}{U_m} \quad (9)$$

Rotational speed variables:
$$p^+ = \frac{p}{f}, \quad q^+ = \frac{q}{f}, \quad r^+ = \frac{r}{f} \quad (10)$$

Longitudinal disturbances:
$$\delta\dot{u}^+ = \frac{\partial\delta u^+}{\partial t^+}, \quad \delta\dot{w}^+ = \frac{\partial\delta w^+}{\partial t^+}, \quad \delta\dot{q}^+ = \frac{\partial\delta q^+}{\partial t^+}, \quad \delta\dot{\theta}^+ = \frac{\partial\delta\theta}{\partial t^+} \quad (11)$$

Lateral disturbances:
$$\delta\dot{v}^+ = \frac{\partial\delta v^+}{\partial t^+}, \quad \delta\dot{p}^+ = \frac{\partial\delta p^+}{\partial t^+}, \quad \delta\dot{r}^+ = \frac{\partial\delta r^+}{\partial t^+}, \quad \delta\dot{\phi}^+ = \frac{\partial\delta\phi}{\partial t^+} \quad (12)$$

Moments of inertial:
$$I_x^+ = \frac{I_x}{0.5\rho U_m^2 ScT^2}, \quad I_y^+ = \frac{I_y}{0.5\rho U_m^2 ScT^2}, \quad I_z^+ = \frac{I_z}{0.5\rho U_m^2 ScT^2}, \quad I_{xz}^+ = \frac{I_{xz}}{0.5\rho U_m^2 ScT^2} \quad (13)$$

Mass, gravity acceleration, and time:
$$m^+ = \frac{m}{0.5\rho U_m ST}, \quad g^+ = \frac{g}{U_m f}, \quad t^+ = \frac{t}{T} \quad (14)$$

where c is the mean chord length, U_m is the mean flapping velocity at the radius of gyration, S is the two-wing area, f is the flapping-wing frequency, ρ is the air density, and T is the flapping period.

The solutions of longitudinal or lateral EoMs are expressed as [17]:

$$\delta x(t) = \mathrm{C}\,\mathrm{diag}(\mathrm{e}^{t\lambda_1}, \mathrm{e}^{t\lambda_2}, \mathrm{e}^{t\lambda_3}, \mathrm{e}^{t\lambda_4})\mathrm{C}^{-1}\delta x(0), \quad (15)$$

where $\delta x(t)$ represents the state vector $\delta x_{long.}(t)$ or $\delta x_{lat.}(t)$, C is a non-singular matrix whose columns are the eigenvectors, λ_i are eigenvalues, and $\delta x(0)$ is the initial condition (*i.e.*, initial disturbances), which is chosen to be the eigenvector ϕ_i corresponding to the eigenvalue λ_i of the i-th mode. Thus, Equation (15) is rewritten as follows:

$$\delta x(t) = \phi_i \mathrm{e}^{t\lambda_i}. \quad (16)$$

2.2. Measured wing kinematics

Fig. 2 shows the coordinate system *Oxyz* that is referenced to determine the wing motion. The y axis points to the right, the x axis points backward, and the z axis points upward. At a local spanwise position, the camber is determined in terms of the middle (θ_m) and full rotation angles (θ_f):

$$\mathrm{Camber}(r) = \frac{h}{c} \times 100\% = \frac{1}{2}\tan(\theta_m - \theta_f) \times 100\%, \quad (17)$$

where h is the mid-chord height, and c is the full-chord length. The θ_f is the angle between the stroke plane and the full-chord line connecting the leading edge and trailing edge, while θ_m is the angle between the stroke plane and the mid-chord line. The geometric angle of attack (α) is the angle between the inflow velocity and the full-chord line. The feather axis aligns on the wing leading edge and moves in the stroke plane (*Oxy*, see Fig. 2). The angle between the feather axis and the y axis is the flapping angle, ψ.

The measured wing kinematics of the SPC and TEC were captured by three synchronized high-speed cameras (Fig. 3a), and reported in [8,36]. Due to the symmetry of the two wings, the process of wing kinematics was implemented only for the right wing, using the direct linear transformation method, DLTv tool [40]. Nine markers were placed on the wing, and four others were located on the body frame, as shown in Fig. 3a. Note the markers in Fig. 3a are enhanced ones for better visibility. The actual markers are smaller and thin to minimize the effect of markers on the wing kinematics measurement. Figs. 3b-d show the time courses of the wing kinematics. Then, the measured wing kinematics were reproduced in the CFD using the nine-term Fourier series function, as follows:

$$f(t) = a_0 + \sum_{\mathrm{k}=1}^{\mathrm{n}=9} \left[a_k \cos(\mathrm{k}2\pi ft) + b_k \sin(\mathrm{k}2\pi ft)\right], \quad (18)$$

where a_0, a_k, and b_k are designated in the user defined function in ANSYS-Fluent to define the fitted angles. Note that the wing kinematics were measured by using the flapping-wing system tethered at a fixture (see Fig. 3a). Since measurement of free-flight wing kinematics is

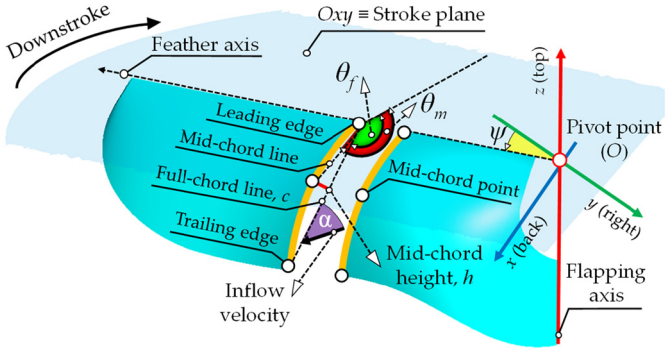

Fig. 2. Definition of the motion on the left wing.

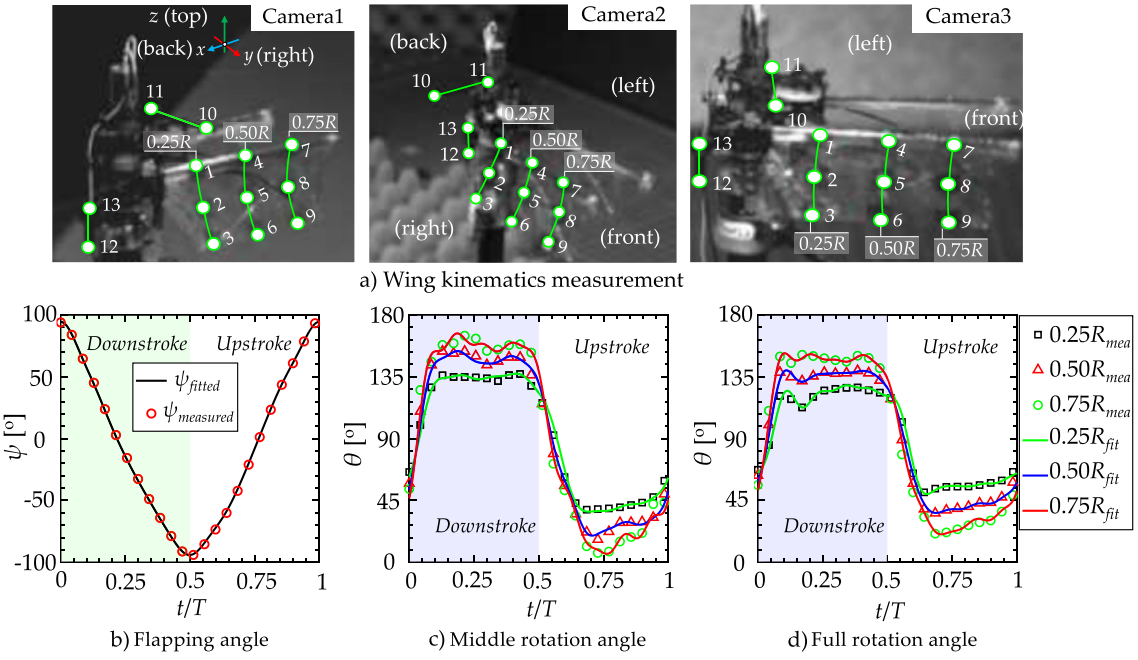

Fig. 3. Measured (mea) and fitted (fit) wing kinematics of the SPC at $0.25R$, $0.5R$, and $0.75R$: a) captured images with enhanced markers by the three high-speed cameras, b) flapping angle, c) middle, and d) full rotation angles. (For interpretation of the colors in the figure(s), the reader is referred to the web version of this article.)

technically more involved, the tethered measurement is widely used to capture the flapping wing kinematics [6,9,14]. The free-flight wing kinematics and tethered wing kinematics are assumed to be close enough.

The fitted wing kinematics of the SPC and TEC are shown in Fig. 4a for the flapping angles, and in Figs. 4b and c for the rotation angles at $0.25R$, $0.5R$, and $0.75R$. The full rotation angle at the wing root ($r/R = 0$) is fixed at 90°, while that at the wing tip ($r/R = 1$) is linearly extrapolated based on those at $0.5R$ and $0.75R$. The time courses of the rotation angles along the wingspan are determined using a cubic spline interpolation. Then, Figs. 4d and e present the three-dimensional (3D) full rotation angles of the two flapping-wing robots.

2.3. Computational fluid dynamics modeling

In this work, we applied a similar meshing method and the same time step size used in the previous works of our group [7,24,25,41], in which the grid independency was verified. Therefore, the presented CFD results can be regarded as converged solutions. Table 2 compares the simulation and measured results of the SPC, in which the cycle-average vertical force Z by the CFD shows about 6% lower than that by the measured one [38]. Since there exists an asymmetric motion between both half-strokes, the horizontal forces X and Y obtained by the CFD method are slightly non-zero.

The wingspan, R is used as the reference length to build the longitudinal (Fig. 5a) and lateral (Fig. 5b) computational domains. For the longitudinal mode, due to the symmetry in the wing motion, the computational domain is a half cylinder measuring $13R$ in length and $13R$ in diameter (Fig. 5a), which is filled by about 2.8 million unstructured tetrahedral elements. The wing is located in the high-density region, such that the wing pivot point is located at the origin O in the wing, while the flapping axis is assigned parallel to the symmetry plane with a distance of 9.5 mm. The domain extends $6R$ from the wing pivot point to the inlet, $7R$ to the outlet, and $6.5R$ to the top. The mesh in the high-density region is finest with about 50% of the total elements, whose maximum edge length is 2.0 mm. Meanwhile, the maximum edge length of elements on the wing surface is 0.5 mm $\sim$ 2% c_{mean} (Fig. 5c). Thus, the mesh size becomes coarser toward the far field, inlet, and outlet. On the other hand, the computational grid domain in the lateral motion is defined by a full 3D cylinder, whose total elements are about 5.2 million tetrahedra, as shown in Fig. 5b. The high-density region has more than 2.6 million elements,

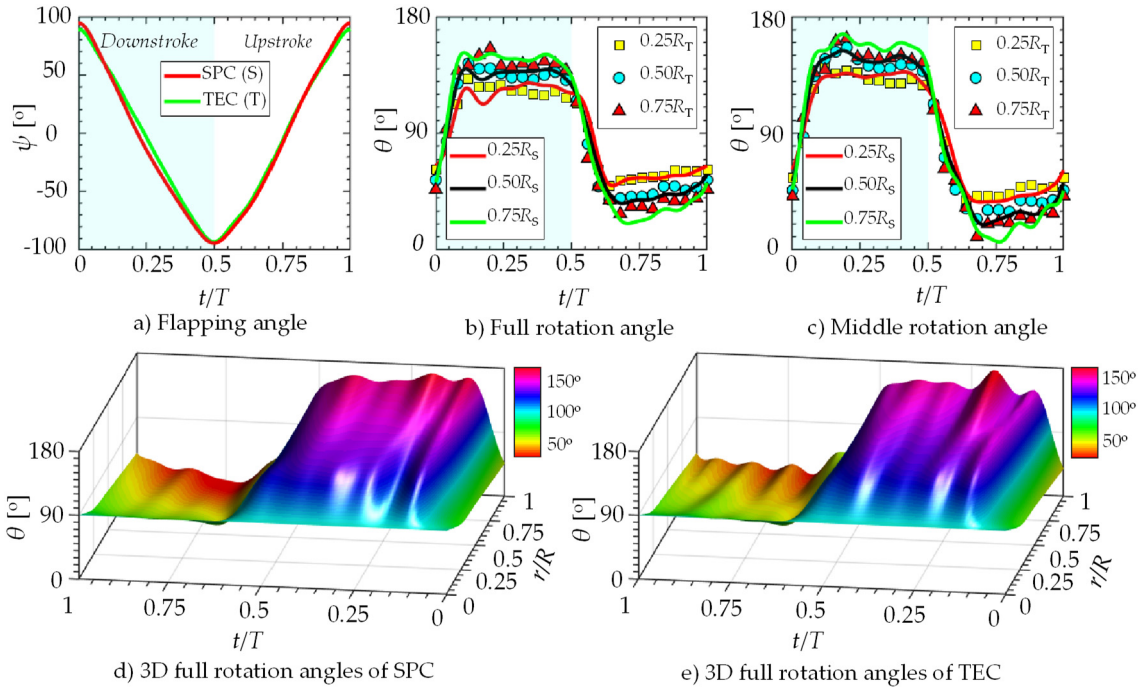

Fig. 4. Fitted wing kinematics of the SPC (S) and TEC (T): a) flapping angle, b) full rotation angles, and c) middle rotation angles at 0.25R, 0.5R, and 0.75R, d), e) 3D full rotation angles along the wingspan of the SPC and TEC, respectively.

Table 2
Force generations of the hovering SPC over one flapping cycle.

Unit: [gf]	Stroke	CFD	Measurement [38]	Δ [%]
Vertical force, Z	*Down*	8.19		
	Up	8.68		
	Total	16.87	18.0	6.23
Front-to-back	*Down*	3.69		
	Up	-3.60		
	Total	0.09	≈ 0	
Side-to-side	*Down*	-1.94		
	Up	0.54		
	Total	-1.40	≈ 0	

whose radius is about 1.4R. The distance between the two wings is 19 mm. Similarly, the maximum edge length on the wing surface is 0.5 mm (Fig. 5c), and that in the high-density region is 2.0 mm. The time step is set to be 1/1,000th of the flapping cycle.

The local Reynolds number, $Re(r)$, along the wingspan is determined in this work using Eq. (19), while Fig. 5e illustrates the Re range of the two systems along the wingspan.

$$Re(r) = \frac{u_{\text{mean}}(r) \times c(r)}{\nu} = \frac{2rf\Phi \times c(r)}{\nu}, \tag{19}$$

where r is the local wing position, $u_{\text{mean}}\ (r)$ is the local spanwise velocity, f is the flapping frequency, $c(r)$ is the local chord length, Φ is the wingbeat amplitude (in rad), and ν is the kinematic viscosity of the air. The Re's of both systems are approximately 10^3 to 10^4 over the wingspan. Although the Re at the outboard wing is relatively high for both FW-MAVs and this is inappropriate to consider as a laminar flow environment, the laminar flow modeling has provided reasonable results in the flapping wing simulation of our previous works [8,24,25,41]. Besides, the estimated cycle-average forces of flapping wings for the Re numbers of 484 to 29,048 were almost the same when they were computed based on the turbulent and laminar flow models [42]. The numerical study on a NACA0012 airfoil at the chord Re numbers in order of 10^4 [43] claimed that the flow pattern computed by the laminar flow simulation was closely predicted to the measurement, while the power coefficients computed by laminar simulation were reasonable in comparison with the measured one. Thus, the laminar flow option is suitable, and is used in this study.

3. Results

3.1. Stability derivatives

To obtain the stability derivatives, the cycle-average forces and moments were first determined for the reference flight at equilibrium. The cycle-average forces and moments of the disturbed flights oscillating from the equilibrium condition were then computed. In particular, the non-dimensional stability derivatives in the longitudinal mode were computed by using the cycle-average X^+, Z^+, and M^+ with

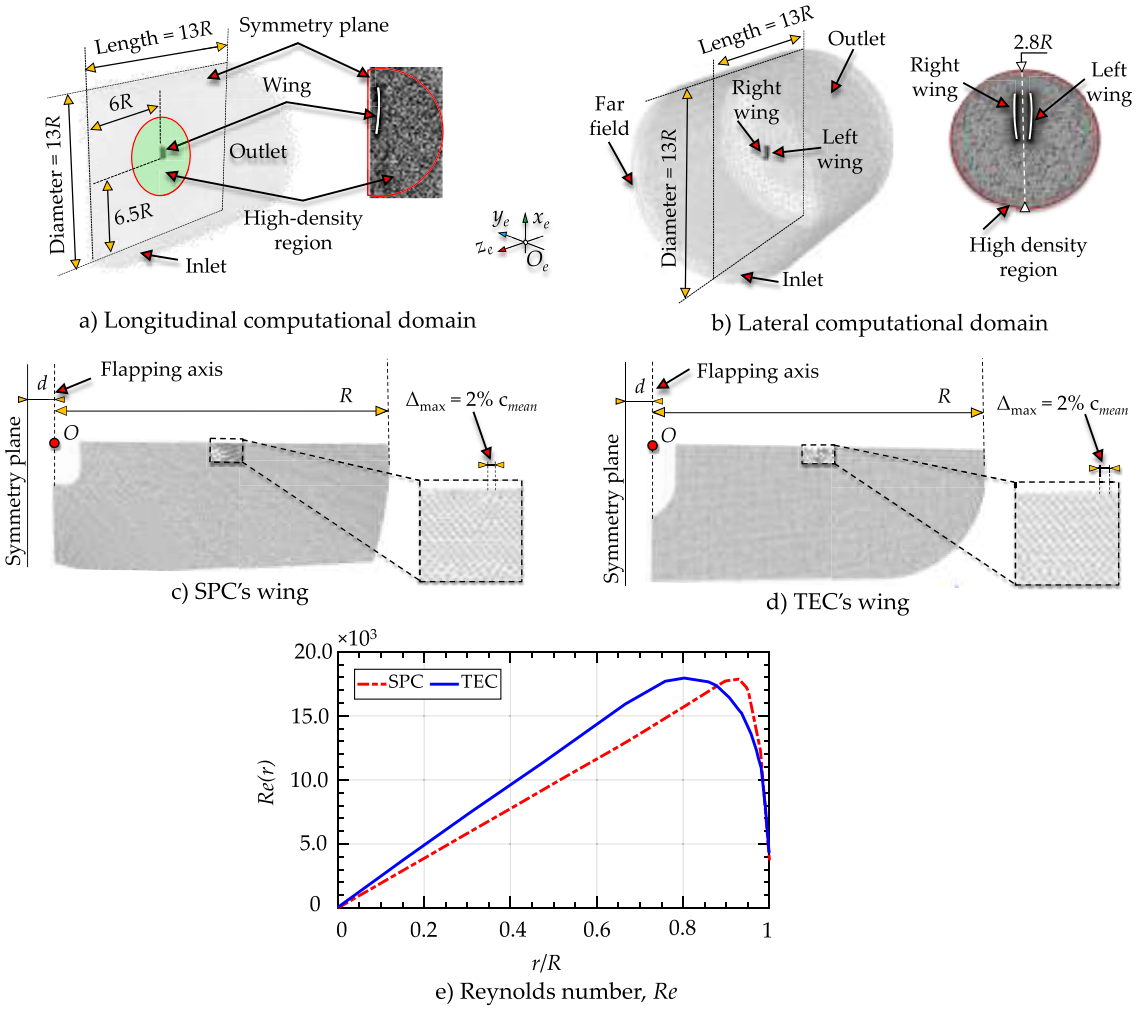

Fig. 5. Modeling of the computational domain for the SPC: a) model for the longitudinal motion, and b) for the lateral motion; c) and d) Mesh configurations for the wing of the SPC and TEC, respectively; e) *Re* number along the wingspan.

respect to u^+, w^+, and q^+. Similarly, the non-dimensional stability derivatives in the lateral mode were calculated from the cycle-average Y^+, L^+, and N^+ for each of v^+, r^+, and p^+. The ranges of disturbance quantities in the translational velocities (u, v, w) were chosen to be ±7% of the mean flapping velocity U_m, while those in the rotational velocities (q, p, r) were ±10% of the flapping frequency, f. These ranges were proven to be small enough for the linearization of EoMs of the flapping wings [15,24,25,44]. For example, in Eq. (20), the derivative X_u^+ is computed using the non-dimensional cycle-average force X_b axis forces in the forward motion ($\Delta u^+_{\min} = -0.07$), and in the backward motion ($\Delta u^+_{\max} = 0.07$), as follows:

$$X_u^+ = \frac{\partial \overline{X}}{\partial u} \cong \frac{X^+\left(u_e^+ + \Delta u^+_{\max}, w_e^+, q_e^+\right) - X^+\left(u_e^+ + \Delta u^+_{\min}, w_e^+, q_e^+\right)}{\Delta u^+_{\max} - \Delta u^+_{\min}}, \tag{20}$$

where u_e^+, w_e^+, and q_e^+ are zero for hovering. The other stability derivatives can be obtained in a similar manner. Table 3 summarizes the longitudinal and lateral stability derivatives of the two vehicles, which are computed at their measured CG location. It is observed that the features of the non-dimensional stability derivatives of the two systems are quite similar, although the wing shape, body mass, and flapping frequencies are different (Table 1). For the longitudinal mode, X_u^+, Z_w^+, and M_u^+ are negative, and their magnitudes are relatively large, while the other derivatives are relatively smaller. For the lateral mode, the derivatives Y_v^+ and N_r^+ are negative, while the L_v^+ is positive. Their magnitudes are relatively larger than the other lateral derivatives. Since the signs and magnitudes of the major derivatives of the two vehicles are similar, this section focuses only on the stability derivatives of the SPC, and it is then explained in the same way for the counterparts of the TEC.

For longitudinal derivatives, Fig. 6 illustrates the effects of the disturbed motions in the u-series (u is perturbed, while v and q are unchanged), v-series (v is perturbed, while u and q are unchanged), and q-series (q is perturbed, while u and v are unchanged) on the forces and pitching moment. When the SPC moves backward with the speed $\Delta u^+_{\max} = 0.07$ (Fig. 6a), the inflow velocity (U) decreases in the downstroke, resulting in a reduction of the vertical force (Z) and horizontal force (X). In other words, the resultant aerodynamic force, F reduces in the downstroke (see Fig. 6a). However, an increase of U in the upstroke causes a reverse augmentation of the F. Thus, the X opposes the backward motion, resulting in the negative speed derivative X_u^+, serving as a damping term. Since the CG is under the stroke plane, the negative force X produces a nose-down pitching, resulting in a negative M_u^+. Meanwhile, the average Z seems not to be affected, explaining the almost zero Z_u^+ (in Table 3).

Table 3
Longitudinal and lateral non-dimensional stability derivatives of the SPC and TEC.

a) Longitudinal motion	Z_{CG}/c_{mean}	*u*-series			*w*-series			*q*-series		
		X_u^+	Z_u^+	M_u^+	X_w^+	Z_w^+	M_w^+	X_q^+	Z_q^+	M_q^+
SPC	-0.75	-1.608	-0.07	-2.227	0.019	-0.899	-0.044	0.149	0.028	-0.059
TEC	-0.60	-1.890	0.10	-1.676	0.060	-0.810	0.024	0.258	-0.007	-0.024
b) Lateral motion	Z_{CG}/c_{mean}	*r*-series			*p*-series			*v*-series		
		L_r^+	Y_r^+	N_r^+	L_p^+	Y_p^+	N_p^+	L_v^+	Y_v^+	N_v^+
SPC	-0.75	-0.077	0.059	-0.850	-0.054	-0.189	0.074	1.725	-1.803	0.254
TEC	-0.60	-0.002	-0.009	-0.763	-0.103	-0.271	0.120	1.075	-1.872	-0.118

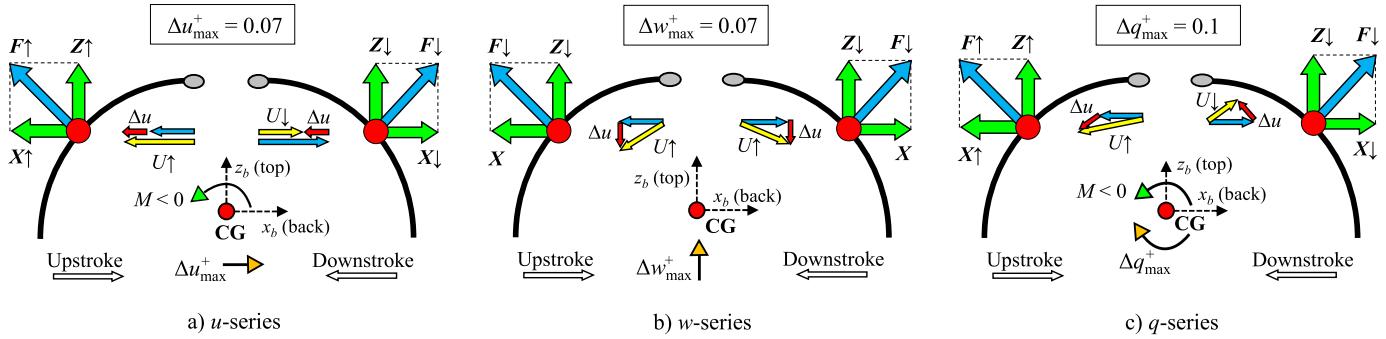

Fig. 6. Effects of disturbed motions in the a) *u*-, and b) *w*-series on the forces (X, Z, and *F*) and moment (*M*): The curved sections stand for cuts of the wing in the downstroke and upstroke (side view). Note that *U* denotes the wing velocity, and Δu represents the inflow due to disturbance.

When the SPC moves upward with the vertical speed $\Delta w^+_{max} = 0.07$ (Fig. 6b), the inflow velocity increases in the two half-strokes. However, Fig. 6b shows that the downward speed component tends to reduce the half cycle-average force Z in both half-strokes. This explains the negative and relatively large derivative Z_w^+, representing the force damping term, while moving upward. Meanwhile, the horizontal force and pitching moment are not significantly affected, resulting in small derivatives X_w^+ and M_w^+, compared to the magnitude of Z_w^+. When the SPC is in a nose-up rotation with the pitch rate $\Delta q^+_{max} = 0.1$ (Fig. 6c), the total inflow U reduces in the downstroke, inducing the reduction of the X and Z, which reduces the pitch-up moment. In contrast, the total inflow U increases in the upstroke, which enhances the forces, resulting in increase of the pitch-down moment. Overall, the SPC is pitched down due to the cycle-average force F being tilted forward when the FW-MAV conducts nose-up rotation, resulting in a negative (nose-down) M_q^+, serving as a pitching damping term. However, its magnitude is insignificant. Meanwhile, the Z_q^+ is almost zero because of the same magnitudes of the pitching rates in the nose-up and nose-down motions. On the other hand, since the measured wing kinematics are slightly asymmetric between two half-strokes, the cycle-average force X is positive and relatively small (Table 2). Thus, the cycle-average derivative X_q^+ is positive.

Next, the constitutions of the main lateral derivatives are presented. The force and moment generation over a flapping cycle are investigated when the FW-MAV is perturbed by the lateral quantities of the *r*-series (*r* is perturbed, while *p* and *v* are unchanged, Fig. 7a), *p*-series (*p* is perturbed, while *r* and *v* are unchanged, Fig. 7b), and *v*-series (*v* is perturbed, while *r* and *p* are unchanged, Fig. 7c). Fig. 7a shows the SPC under the positive yawing rotation ($\Delta r^+_{max} = 0.1$). Due to the change in the total inflow velocity over the downstroke, the drag, D (opposite to the wing motion) increases on the right wing, but reduces on the left wing, creating a negative yawing moment N (Fig. 7a1). Furthermore, in the upstroke, because D enhances the drag on the left wing and reduces that on the right wing (Fig. 7a2), negative yaw moment is also produced. Therefore, the derivative N_r^+ is negative, and relatively larger than the other derivatives in the *r*-series, representing a damping term in the yawing motion. In Fig. 7b, the SPC is under a positive rolling motion ($\Delta p^+_{max} = 0.1$). The total inflow U on the right wing decreases in the first half of the downstroke, and increases in the second half, as shown in Fig. 7b1. On the other hand, on the left wing, U increases in the first half, and decreases in the second half of the downstroke. Hence, the increased half-cycle-average force Y points to the right. Additionally, due to the CG being below the stroke plane, the rolling moment L is negative in the downstroke. Meanwhile, the negative rolling moment is also produced in the upstroke due to the increased half-cycle-average force Y, which directs toward the right (Fig. 7b2). Therefore, the cycle-average derivative L_p^+ is negative, which is known as the damping term in roll rotation. However, its magnitude is relatively small to stabilize the system. Additionally, the asymmetry of the measured wing kinematics causes the differences of side force Y generation for both half-strokes, which results in the negative cycle-average force Y (Table 2). Thus, the cycle-average derivative Y_p^+ is negative.

In Fig. 7c, when the SPC is in sideward motion ($\Delta v^+_{max} = 0.07$), the total inflow U on the right wing increases in the first half of the downstroke, resulting in the increase of D (Fig. 7c1). In the second half of the downstroke, the reduced total velocity U decreases D, which produces the negative horizontal-side force Y in the downstroke. This tendency is reversed for the left wing. The drag reduces in the first half stroke, and increases in the second half stroke, which also produces the negative force Y. Then, the generation of drag is explained in a similar manner to the upstroke motion, in Fig. 7c2. The drag on the right wing increases in the first half of the upstroke, and decreases in the second half, which creates the negative force Y. Then, on the left wing, the drag, which is compared to that from the right wing, is reversely produced in the two halves of the upstroke, producing a negative Y. Thus, the total average Y is negative and relatively large, which makes the vehicle tend to move to the left. Therefore, the non-dimensional derivative Y_v^+ becomes negative, and relatively large. Furthermore, since the CG is below the stroke plane, the pointing-left force Y produces a positive and relatively large L_v^+.

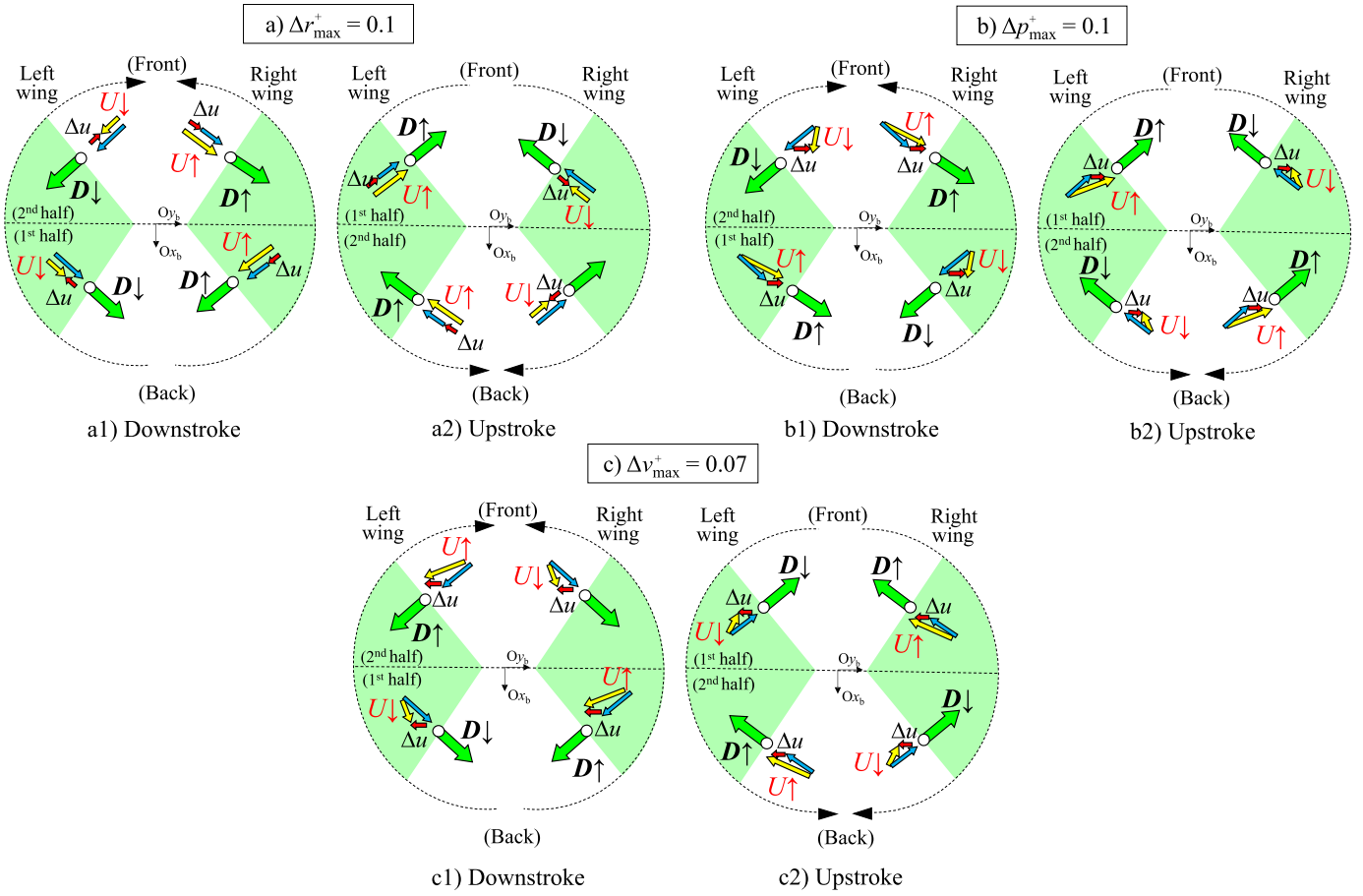

Fig. 7. Force and moment generation in the downstroke and upstroke by the disturbed motions in the a) *r*-series, b) *p*-series, and c) *v*-series (top view). Note that U denotes the wing velocity, and Δu represents the inflow due to disturbance.

3.2. Eigenvalues and eigenvectors

This section presents the characteristics in the longitudinal and lateral motions for the SPC. Then, they are compared with those of the TEC. Equation (21) shows the non-dimensional longitudinal system matrices of the two FW-MAVs, which are filled out by the cycle-average derivatives and their morphological parameters.

$$A_{SPC\_long} = \begin{bmatrix} -0.0588 & 0.0007 & 0.0054 & 0.0660 \\ -0.0026 & -0.0328 & 0.0010 & 0 \\ -1.2764 & -0.0252 & -0.0338 & 0 \\ 0 & 0 & 1 & 0 \end{bmatrix} \quad \& \quad A_{TEC\_long} = \begin{bmatrix} -0.0478 & 0.0015 & 0.0065 & 0.0450 \\ 0.0025 & -0.0205 & -0.0002 & 0 \\ -0.2357 & 0.0033 & -0.0034 & 0 \\ 0 & 0 & 1 & 0 \end{bmatrix} \tag{21}$$

Using the analysis of eigenvalues and eigenvectors, the estimated solutions of the longitudinal EoM are expressed in polar forms (Table 4) for the SPC and TEC. The modes of motion are determined based on the eigenvalues. For example, there are two negative real roots, in which the root with the relatively larger magnitude represents the fast subsidence mode, while the smaller one stands for the slow subsidence mode. A pair of complex conjugate roots with a positive real part represent a divergent oscillation mode. Based on the computed eigenvalues, the physical characteristics of each mode of the motion are revealed. For example, the period of the divergence oscillation mode, the time to double or halve the initial perturbations are revealed. The magnitudes of the eigenvalues of the SPC are about twice larger than those of the TEC (Table 4). This means that the time response of SPC is faster than that of TEC.

Table 5 uses the non-dimensional times of t_{double} or t_{half} to describe the time when the initial disturbance quantities halve or double in their magnitudes in each mode of motion. Note that the reference time used to compute non-dimensional quantities is the wingbeat period: $T_{\text{SPC}} = {f_{\text{SPC}}}^{-1} = 43.3$ ms, and $T_{\text{TEC}} = {f_{\text{TEC}}}^{-1} = 33.3$ ms. For example, on the fast subsidence mode, for the SPC, the time to halve the initial disturbances is 1.5 wingbeats, representing 0.06 s. Meanwhile, that of the TEC is about 2.9 wingbeats, or about 0.09 s. This indicates that the SPC is stabilized about 33.3% faster than the TEC on the fast subsidence mode. Meanwhile, the stability for the slow subsidence mode of the SPC is achieved after 21 wingbeats, representing 0.91 s, and the slow subsidence mode of the TEC is stabilized after about 34 wingbeats. This reveals that for the slow subsidence mode, the SPC becomes stable 20% faster than the TEC. For the divergence oscillation mode, the period of this divergence mode for the SPC is about 16.4 times of the wingbeat, or about 0.71 s. Meanwhile, that for the TEC is about 33.3 times the flapping cycle, or about 1.10 s. The initial disturbances of the SPC are doubled in 3.7 wingbeats, or about 0.16 s. Meanwhile, the TEC doubles its first disturbances after 7.5 wingbeats, accounting for 0.25 s. This indicates that in the oscillation mode, the SPC is 36% more unstable than the TEC.

Table 4
Eigenvalues of two FW-MAVs in longitudinal motion.

	Eigenvalues		
	Fast subsidence ($\lambda_1 = n \pm 0i$)	Divergence oscillation ($\lambda_{2,3} = n \pm \omega i$)	Slow subsidence ($\lambda_4 = n \pm 0i$)
SPC	-0.464	0.186 ± 0.383i	-0.033
TEC	-0.235	0.092 ± 0.191i	-0.020

Table 5
Non-dimensional time for the SPC and TEC according to their modes in longitudinal motion.

	z_{CG}/c	T (ms)	Fast subsidence	Divergence oscillation		Slow subsidence
			$t_{half} = \ln 2 \times \lvert Real(\lambda_1)\rvert^{-1}$	$T_{mode\_long.} = 2\pi/\omega$	$t_{double} = \ln 2 \times \lvert Real(\lambda_{2,3})\rvert^{-1}$	$t_{half} = \ln 2 \times \lvert Real(\lambda_4)\rvert^{-1}$
SPC	-0.75	43.4	1.5 (0.06 s)	16.4 (0.71 s)	3.7 (0.16 s)	21.1 (0.91 s)
TEC	-0.60	33.3	2.9 (0.09 s)	32.9 (1.10 s)	7.5 (0.25 s)	33.9 (1.13 s)

Table 6
Eigenvalues of the two FW-MAVs in lateral motion.

	Eigenvalues		
	Fast subsidence ($\lambda_1 = n \pm 0i$)	Divergence oscillation ($\lambda_{2,3} = n \pm \omega i$)	Slow subsidence ($\lambda_4 = n \pm 0i$)
SPC	-1.636	0.160 ± 0.340i	-0.417
TEC	-0.892	0.074 ± 0.164i	-0.209

Table 7
Non-dimensional time for the SPC and TEC according to their modes in lateral motion.

	z_{CG}/c	T (ms)	Fast subsidence	Divergence oscillation		Slow subsidence
			$t_{half} = \ln 2 \times \lvert Real(\lambda_1)\rvert^{-1}$	$T_{mode\_lat.} = 2\pi/\omega$	$t_{double} = \ln 2 \times \lvert Real(\lambda_{2,3})\rvert^{-1}$	$t_{half} = \ln 2 \times \lvert Real(\lambda_4)\rvert^{-1}$
SPC	-0.75	43.4	0.4 (0.02 s)	18.5 (0.80 s)	4.3 (0.19 s)	1.7 (0.07 s)
TEC	-0.60	33.3	0.8 (0.03 s)	38.3 (1.28 s)	9.4 (0.31 s)	3.3 (0.11 s)

Tables 6 and 7 show the solutions of the lateral EoM for the SPC and TEC based on the eigenvalue analysis. There are three modes in the lateral motion: one fast subsidence mode, one slow subsidence mode, and one divergence mode, which are identically determined as those in the longitudinal motion. The magnitudes of the lateral eigenvalues of the SPC are about twice larger than their counterparts of the TEC (Table 6). This means that the time responses of the SPC are faster than those of the TEC for the lateral motion. The non-dimensional forms of the lateral system matrices for the SPC and TEC are then written as follows:

$$A_{SPC\_lat} = \begin{bmatrix} -0.0659 & -0.0069 & 0.0022 & -0.0660 \\ 0.8873 & -0.0351 & 0.0339 & 0 \\ 0.3393 & 0.1470 & -1.6330 & 0 \\ 0 & 1 & 0 & 0 \end{bmatrix} \quad \& \quad A_{TEC\_lat} = \begin{bmatrix} -0.0442 & -0.0064 & -0.0002 & -0.0450 \\ 0.1501 & -0.0145 & 0.0004 & 0 \\ -0.1383 & 0.1399 & -0.8889 & 0 \\ 0 & 1 & 0 & 0 \end{bmatrix} \tag{22}$$

Table 7 shows that the time of doubling the initial disturbance quantities in the divergence mode is about 0.19 s for the SPC and about 0.31 s for the TEC. It means that the SPC is 39% more unstable in the divergence mode. Meanwhile, the magnitudes of the initial disturbance quantities in the fast subsidence mode and the slow subsidence mode of the SPC decrease by half in 0.02 s and 0.07 s, respectively, and those of the TEC are 0.03 s and 0.11 s, respectively. This implies that the convergence speed of the fast subsidence mode and the slow subsidence mode by the SPC are about 33.3% and 36.4% faster, respectively than those by the TEC.

The initial perturbations from the reference flight condition, $\delta x(0)$ is chosen as the eigenvector, ϕ_i corresponding to each of the eigenvalue λ_i, which satisfies Eq. (15). Each eigenvalue and the corresponding eigenvector identify a natural mode, and the linear combination of these natural modes represents the motion of the system. In Table 8, the eigenvectors are correspondingly displayed in polar forms for each of λ_i in the longitudinal and lateral motions for the two FW-MAVs. Meanwhile, the motions of these modes using Eq. (16): $\delta x(t) = \phi_i\, e^{t\lambda i}$ are demonstrated in section 3.4. Note that the eigenvectors of all modes are scaled such that $\delta\theta$ and $\delta\phi$ equal one radian only for convenient comparison. The magnitudes of eigenvectors of the SPC and the TEC are different, due to the parameters and derivatives used to determine the EoMs. However, their signs are identical for the major disturbance variables in each mode. For the longitudinal motion (Table 8a), in the fast subsidence mode and the divergence mode, the initial disturbances of the backward-to-forward transition (δu^+) and the pitching rotation (δq^+) are relatively larger than that of the vertical transition (δw^+). Meanwhile, δw^+ is the largest in the slow subsidence mode. Hence, the vertical transition is decoupled from the horizontal translation and pitching rotation in the longitudinal motion. For the lateral motion (Table 8b), in the fast subsidence mode, the initial disturbance is mainly characterized by the yawing rotation (δr^+), which is significantly larger than the sideward translation (δv^+) and the rolling rotation (δp^+). In the slow subsidence mode and the divergence oscillation mode, the initial disturbances of the δv^+ and the rolling rotation δp^+ are relatively larger than that of the variable δr^+. Thus, in the lateral motion, the sideward translation and rolling rotation are decoupled from the yawing rotation.

3.3. Effects of stability derivatives on eigenvalues

To investigate the effects of stability derivatives on the solutions of EoM, this section estimates the trend of eigenvalues when each of the derivatives is individually varied, while the other derivatives are kept at their original values. To begin with, Fig. 8 presents the root

Table 8
Eigenvectors of the two systems in a) longitudinal, and b) lateral motions.

a) Longitudinal motion		Eigenvectors							
		δu^+		δw^+		δq^+		$\delta\theta$	
		Value	Phase angle	Value	Phase angle	Value	Phase angle	Value	Phase angle
SPC	Fast subsidence	1.6×10^{-1}	180°	2.0×10^{-4}	0°	4.6×10^{-1}	180°	1.0	0°
	Slow subsidence	1.1×10^{0}	0°	5.4×10^{1}	180°	3.3×10^{-2}	180°	1.0	0°
	Divergence Oscillation	1.5×10^{-1}	56°	1.6×10^{-3}	30°	4.3×10^{-1}	64°	1.0	0°
TEC	Fast subsidence	2.3×10^{-1}	180°	2.5×10^{-3}	0°	2.4×10^{-1}	180°	1.0	0°
	Slow subsidence	5.6×10^{-1}	180°	3.9×10^{1}	180°	2.0×10^{-2}	180°	1.0	0°
	Divergence Oscillation	1.9×10^{-1}	52°	2.3×10^{-3}	65°	2.1×10^{-1}	64°	1.0	0°
b) Lateral motion		Eigenvectors							
		δv^+		δp^+		δr^+		$\delta\phi$	
		Value	Phase angle	Value	Phase angle	Value	Phase angle	Value	Phase angle
SPC	Fast subsidence	0.075	180°	1.636	180°	79.23	0°	1.0	0°
	Slow subsidence	0.180	0°	0.417	180°	0.000	180°	1.0	0°
	Divergence Oscillation	0.165	55°	0.376	65°	0.053	85°	1.0	0°
TEC	Fast subsidence	0.529	0°	0.889	180°	1882.8	0°	1.0	0°
	Slow subsidence	0.270	0°	0.209	180°	0.098	180°	1.0	0°
	Divergence Oscillation	0.223	52°	0.180	66°	0.030	13°	1.0	0°

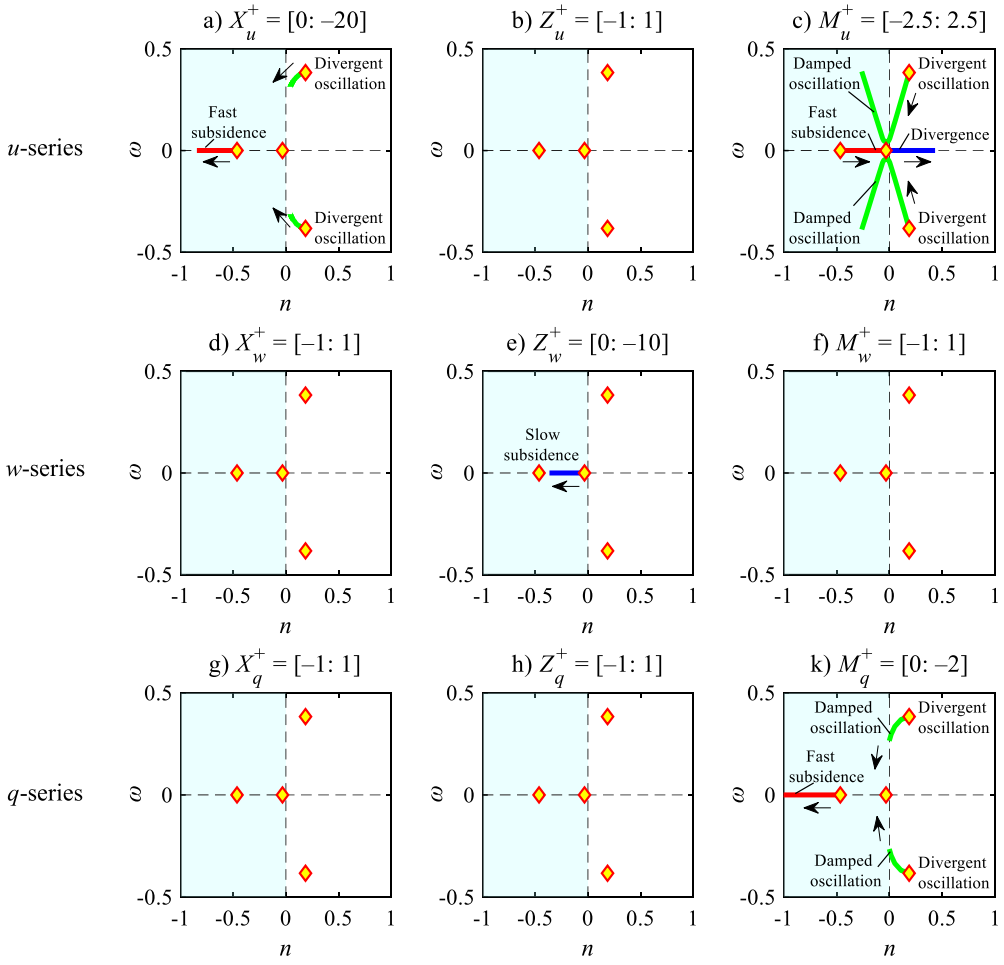

Fig. 8. Root loci showing the effect of derivatives on the roots of the longitudinal EoMs for the SPC. The yellow diamonds with red outlines represent the roots computed for their defined derivatives. The arrows point out the trends of the roots when the derivatives are changed. The green colors represent the divergent oscillation modes, the blue colors stand for the slow subsidence mode, and the red colors denote the fast subsidence mode. The real part of a root is denoted by n, while the imaginary part is represented by ω. Roots moving towards the left are more stable.

locus of the longitudinal EoM when the derivatives of u-series (Figs. 8a-c), v-series (Figs. 8d-f), and q-series (Figs. 8g-k) are investigated. The numbers in bracket in Figs. 8 and 9 stand for the range of change in each variable. The influences of the longitudinal derivatives Z_u^+ (Fig. 8b), X_w^+ (Fig. 8d), M_w^+ (Fig. 8f), X_q^+ (Fig. 8g), and Z_q^+ (Fig. 8h) on the eigenvalues are observed to be insignificant. Meanwhile,

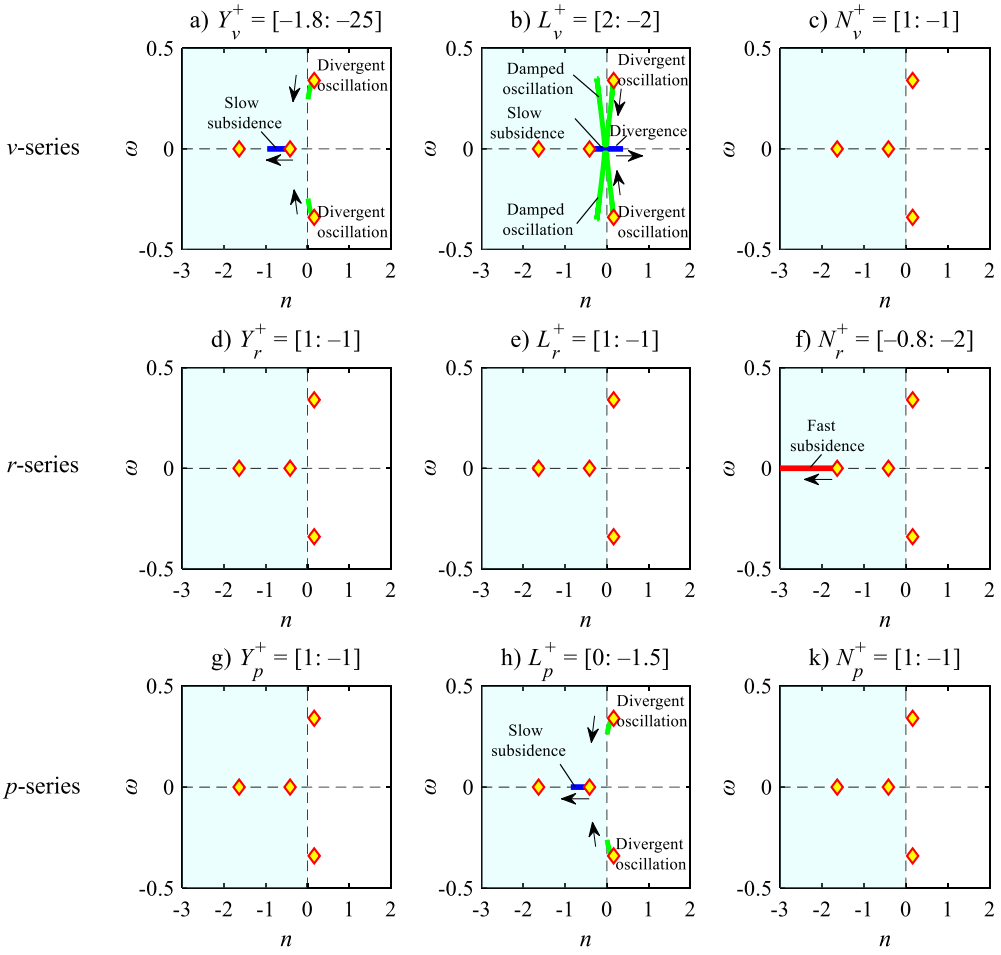

Fig. 9. Root loci showing the effect of derivatives on the roots of the lateral EoMs for the SPC. The yellow diamonds with red outlines represent the roots computed for their defined derivatives. The arrows point out the trends of the roots when the derivatives are changed. The green colors represent the divergent oscillation modes, the blue colors stand for the slow subsidence mode, and the red colors denote the fast subsidence mode. The real part of the roots is denoted by n, while the imaginary part is represented by ω. Roots moving towards the left are more stable.

when the X_u^+ (Fig. 8a), M_u^+ (Fig. 8c), Z_w^+ (Fig. 8e), and M_q^+ (Fig. 8k) are changed, the roots are considerably affected. For X_u^+ (Fig. 8a), the divergence oscillation modes become closer to the vertical dash line, representing the smaller magnitude of the real parts of the complex roots, when X_u^+ decreases from 0 to -20. This means that the instability in this mode is reduced for the decrease of X_u^+. It is also found that the fast subsidence mode moves to the left of the plot due to the change in X_u^+, which makes this mode also stabilize faster. Meanwhile, there is no effect on the slow subsidence mode. Thus, X_u^+ serves as a damping term in the divergence mode and the fast subsidence mode. However, the actual magnitude of X_u^+ is relatively small to stabilize these modes.

When M_u^+ increases from -2.5 to 2.5 (Fig. 8c), the positive real parts of the complex roots become negative, which damps the divergence oscillation modes. However, the negative real root with larger magnitude becomes smaller (still negative), while the one with smaller magnitude becomes larger and positive. This means that the stable fast subsidence mode becomes the stable slow subsidence mode, whereas the slow subsidence mode becomes divergent. Therefore, the effect of M_u^+ on the longitudinal stability is dominant for the SPC. In addition, Fig. 8c shows that the negative and larger M_u^+ makes the divergence oscillation mode more unstable. However, its magnitude depends on the CG location (see section 3.1). For the SPC, the CG is located at 0.75c below the stroke plane, which is farther than that of 0.6c for the TEC. Therefore, the negative M_u^+ of the SPC is about 33% larger than that of the TEC (Table 3). It results in the faster unstable longitudinal oscillation mode of the SPC. This agrees with the report by Au et al. [24] on the influence of CG on the longitudinal stability of the FW-MAV. Meanwhile, in Fig. 8e, the influence of Z_w^+ is noticeable only in the slow subsidence mode. The negative real part of the smaller root becomes larger for decreasing Z_w^+ from 0 to -10. Therefore, the slow subsidence mode is stabilized faster. Furthermore, Fig. 8k shows the changes of the roots, when M_q^+ decreases from 0 to -2. The fast subsidence mode becomes stable more quickly, since the root moves to the left. In addition, the divergence mode is damped. However, its real parts are almost zero, representing a slowly damped mode. This means that when the M_q^+ is around -2 (while the other derivatives are at their originals), the longitudinal motion of the SPC is totally stable with one faster subsidence mode, one slow subsidence mode, and one slow damped oscillation mode (see Fig. 8k).

Fig. 9 shows the effects of lateral stability derivatives on the system poles for the v-series, r-series, and p-series. The roots of the lateral EoM are not affected by the N_v^+ (Fig. 9c), Y_r^+ (Fig. 9d), L_r^+ (Fig. 9e), Y_p^+ (Fig. 9g), and N_p^+ (Fig. 9k) when their derivatives are changed. Meanwhile, the Y_v^+ (Fig. 9a), L_v^+ (Fig. 9b), N_r^+ (Fig. 9f), and L_p^+ (Fig. 9h) show the significant influences. For example, when Y_v^+ reduces from -1.8 to -25 (Fig. 9a) and L_p^+ decreases from 0 to -1.5 (Fig. 9h), the tendencies in changing the roots are quite similar for the two cases. The divergence mode converts to the slow damped oscillation mode, and the slow subsidence mode becomes stable faster. Meanwhile,

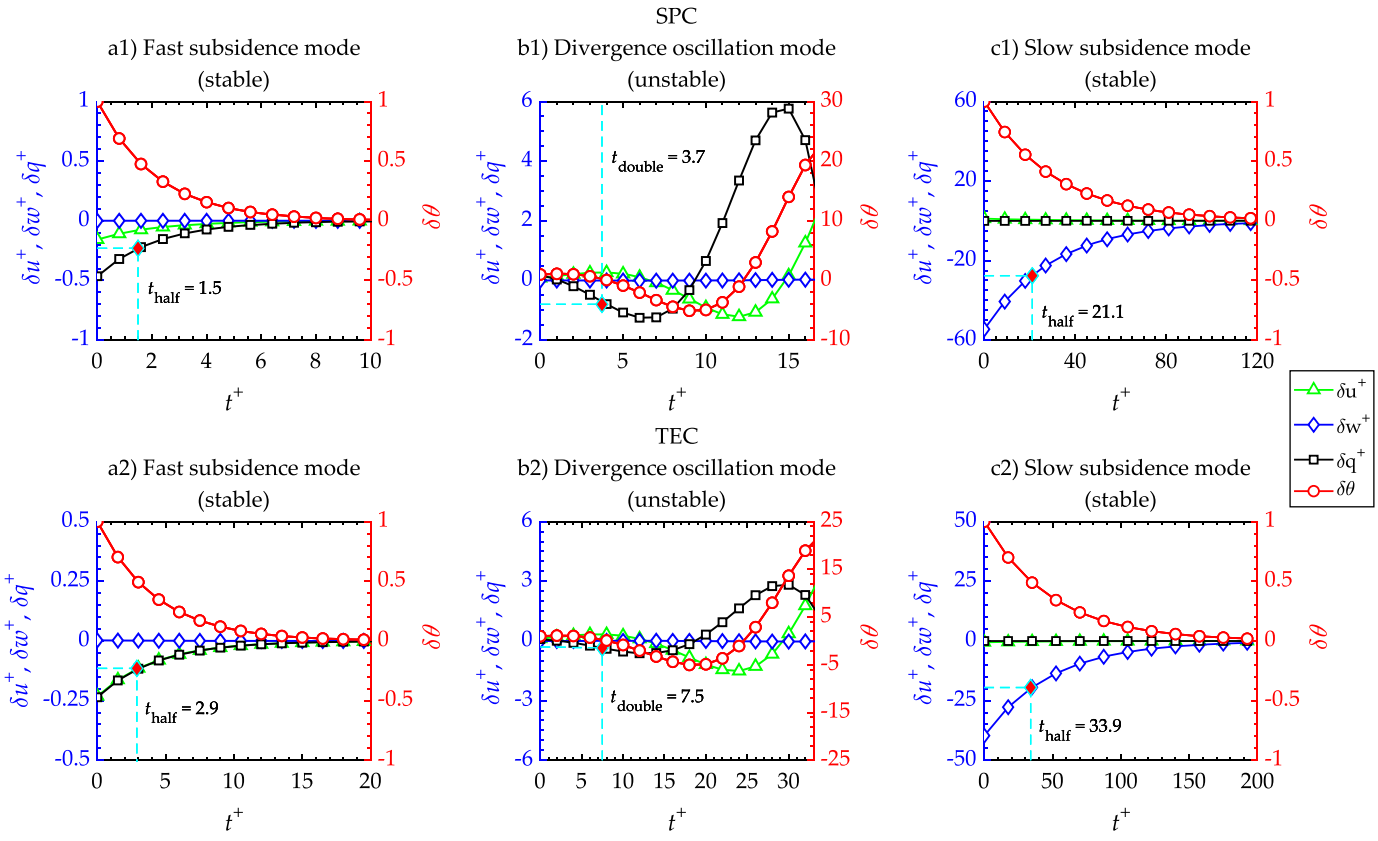

Fig. 10. Eigenvectors in each mode of the longitudinal motion of the SPC (a1)-(c1) and the TEC (a2)-(c2). The left vertical axes are the disturbance quantities of δu^+, δw^+, and δq^+, while the right vertical axes denote the pitch angle, $\delta\theta$.

the fast subsidence modes are almost unaffected. When decreasing from -0.8 to -2, the N_r^+ enhances only the speed of stabilizing the fast subsidence mode (Fig. 9f).

In contrast, as shown in Fig. 9b, the L_v^+ reduces from 2 to -2, the divergence mode becomes the damped oscillation mode, and the slow subsidence mode becomes divergent. This means that the larger L_v^+ makes the divergence oscillation mode more unstable. However, the magnitude of L_v^+ depends on the distance from the stroke plane to the CG location (discussed in section 3.1). For the SPC, the CG is located at $0.75c$, which is further than $0.6c$ of the TEC. Therefore, the L_v^+ of the SPC is about 60.5% larger than that of the TEC. It makes the lateral oscillation mode of the SPC become quicker unstable. This matches with our previous finding about the relationship between the stable zone of CG location and the lateral stability derivative L_v^+, as reported in [25].

In summary, for the longitudinal motion, the two damping-force derivatives, X_u^+ and Z_w^+, the damping-moment derivative M_q^+, and the instability-causing pitching moment derivative with respect to the horizontal translation velocity, M_u^+ are the major stability derivatives that determine the longitudinal stability characteristics. For the lateral motion, the damping-force derivative Y_v^+, the two damping-moment derivatives, L_p^+ and N_r^+, and the instability-causing rolling moment derivative with respect to the side translation velocity, L_v^+ predominantly affect the lateral stability characteristics. The damping derivatives are definitely beneficial for the stability of the FW-MAV. However, their actual magnitudes are not large enough to stabilize the unstable mode. Therefore, without a feedback control, the two FW-MAVs are inherently unstable.

3.4. Time transients of disturbances

Fig. 10 displays the characteristic transients of the longitudinal disturbance quantities for the three modes of motion for the SPC (Figs. 10a1-c1) and the TEC (Figs. 10a2-c2). First, in the fast subsidence modes (Figs. 10a1 and a2), the disturbed terms of δq^+ and δu^+ begin with the negative values, whilst the $\delta\theta$ has a positive value. This means that the two FW-MAVs perform forward translation ($\delta u^+ < 0$) and nose-down rotation ($\delta q^+ < 0$), while the body is pitched up ($\delta\theta = 1$) at the beginning. The SPC gains stability in the fast subsidence mode after 10 wingbeats (0.43 s) in Fig. 10a1, while the equilibrium state of the TEC is obtained after 20 wingbeats (0.67 s) in Fig. 10a2. Therefore, the fast subsidence mode of the SPC is stabilized about 35% faster than that of the TEC. Fig. 8k shows that when decreasing its value, the M_q^+ predominantly affects the fast subsidence mode and the divergence mode. Therefore, the larger damping-moment derivative M_q^+ for the SPC (Table 3a) induces its characteristic transients of perturbation to stabilize faster than those of the TEC on the fast subsidence mode. However, its magnitude is quite small to damp out the two divergence modes.

On the divergence mode, Figs. 10b1 and b2 illustrate the first non-dimensional cycle of the divergence mode of each FW-MAV correspondingly, *i.e.*, 16.4 wingbeats (0.71 s) for the SPC, and 32.9 wingbeats (1.10 s) for the TEC. Overall, the trends of disturbance quantities are similar for both FW-MAVs. For the first half of the cycle of both FW-MAVs, the backward translation ($\delta u^+ > 0$) is coupled with the nose-down pitching motion ($\delta q^+ < 0$). Meanwhile, for most of the remaining half cycle, the forward translation ($\delta u^+ < 0$) is coupled with the nose-up pitching motion ($\delta q^+ > 0$). In addition, the variable δq^+ of the SPC is relatively larger than that of the TEC, which is clearly

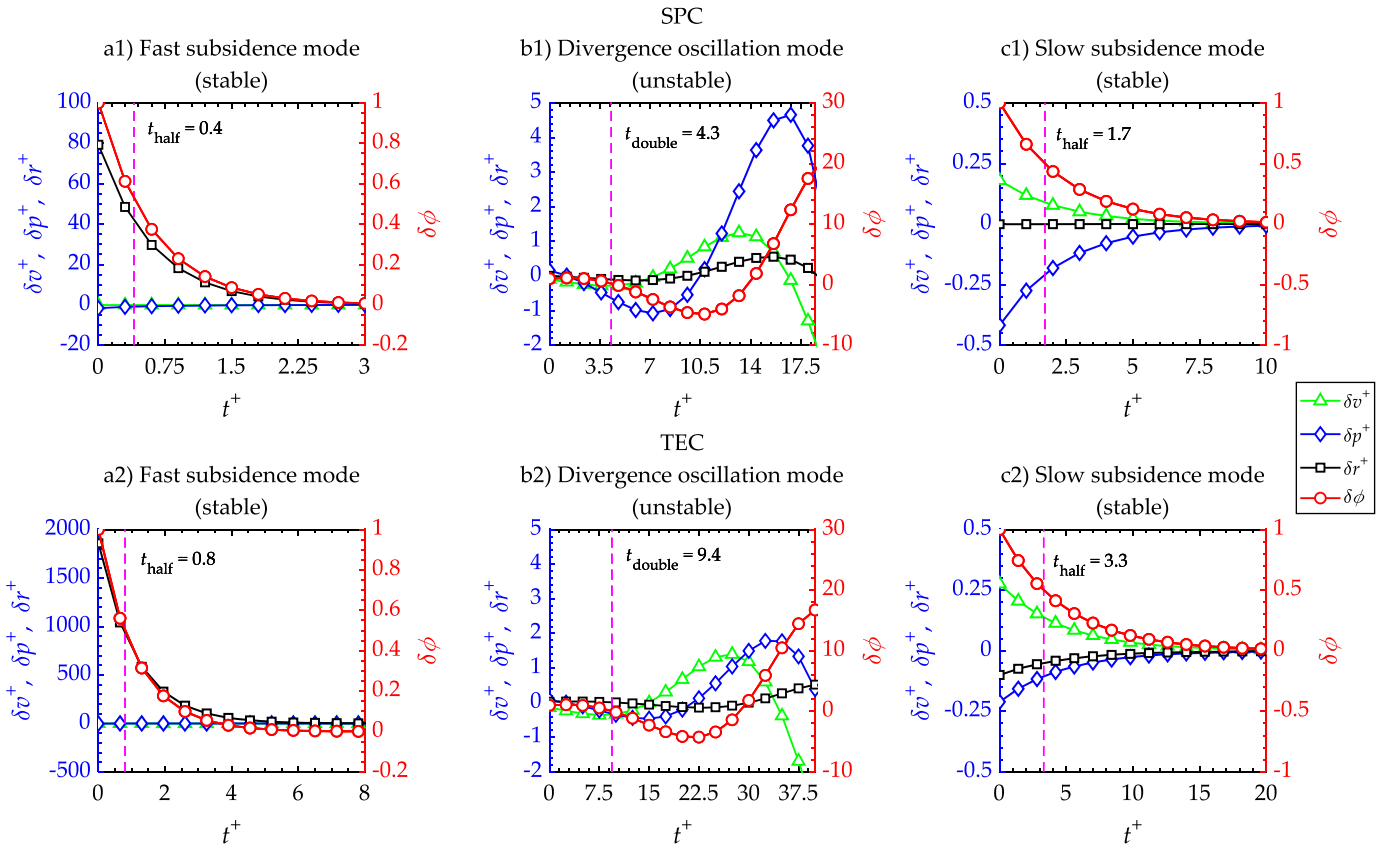

Fig. 11. Eigenvectors in each mode of the lateral motion of the SPC (a1)-(c1) and the TEC (a2)-(c2). The left vertical axes are the disturbance quantities of δv^+, δp^+, and δr^+, while the right vertical axes denote the $\delta\phi$.

shown at the end of the cycle in Figs. 10b1 and b2, while the magnitudes of the other variables are almost similar. Since the M_u^+ of the SPC is larger than that of the TEC, by about 33% (comparing their magnitudes of -2.23 and -1.68, respectively (see Table 3a), the influence of the horizontal translation (u) on the pitching rotation (M) of the SPC is relatively larger as well. This causes more instability for the SPC compared to the TEC (Fig. 8c), explaining the larger δq^+. Thus, as shown in Figs. 10b1 and b2, when the times for doubling the initial magnitudes of disturbances (t_{double}) are compared, in the divergence mode, the SPC becomes unstable 36% faster than the TEC.

For the slow subsidence mode of the longitudinal mode, the vertical transition (δw^+) is the main variable (Figs. 10c1 and c2). While the FW-MAVs descend ($\delta w^+ < 0$) at $t^+ = 0$, the two other terms (δu^+ and δq^+) are negligible. In particular, the descending rate is zero after 120 wingbeats for the SPC (5.2 s), while the TEC needs 200 wingbeats (6.67 s) to achieve convergence. Hence, the stability of the SPC on the slow subsidence mode is about 22% faster than that of the TEC. Meanwhile, the effect of the damping-force derivative Z_w^+ on the roots in Fig. 8e shows that the larger magnitude of Z_w^+ causes the slow subsidence mode to converge faster. As a result, the larger Z_w^+ of the SPC (Table 3a) contributes to quicker stabilization of the slow subsidence mode. However, since the magnitude of Z_w^+ is quite small for both FW-MAVs, this slow subsidence mode still takes a long time to establish convergence.

For the lateral motion, Fig. 11 shows the characteristic transients of the disturbance quantities for the three modes of the motion for the SPC (Figs. 11a1-c1) and the TEC (Figs. 11a2-c2). In Figs. 11a1 and a2, the fast subsidence modes of both FW-MAVs demonstrate that the δr^+ is the mainly disturbed motion, and its magnitude is positive and relatively large, whereas the other variables are smaller. This reveals that the two FW-MAVs perform a positive yawing rotation (counter-clockwise from the top view). However, the initial yaw variable δr^+ of the TEC ($\approx$ 1,900) is about two orders larger than that ($\approx$ 80) of the SPC. The SPC gains stability on the fast subsidence mode after 3 wingbeats (0.13 s) (see Fig. 11a1), while that of the TEC is about 7 wingbeats (0.23 s) (see Fig. 11a2). As a result, the fast subsidence mode of the SPC converges about 44% faster than that of the TEC. In addition, the larger magnitude of the damping-moment derivative N_r^+ of the SPC (Table 3a) is beneficial for the convergence speed in the fast subsidence mode, which is shown in Fig. 9f. This explains the faster stability for the SPC, compared to that of the TEC, in the fast subsidence mode.

Figs. 11b1 and b2 show the first non-dimensional cycle of the divergence oscillation mode of the SPC and TEC, respectively, *i.e.*, 18.5 wingbeats (0.80 s) for the SPC, and 38.3 wingbeats (1.28 s) for the TEC. However, the two trends of disturbance quantities are similar. Overall, for the first half of the cycle of both FW-MAVs, the left-side translation ($\delta v^+ < 0$) is coupled with the right-roll rotation ($\delta p^+ < 0$), whilst the yaw rotation slightly oscillates at the end of the cycle (see Figs. 11b1 and b2). Furthermore, when compared with that of the TEC, the disturbed rolling term δp^+ of the SPC is nearly double, especially at the end of the first cycle. Meanwhile, the magnitudes of the other variables are almost the same. Since the L_v^+ of the SPC is about 60% larger than that of the TEC (when the magnitudes of 1.73 and 1.08, respectively, are compared in Table 3b), the effect of the sideward translation (v) on the rolling rotation (L) is relatively larger than that of the TEC. This causes instability of the SPC, accounting for about 39% faster instability than that of the TEC, when the times for doubling the initial magnitudes of disturbances (t_{double}) in the divergence oscillation mode of the two FW-MAVs are compared.

The slow subsidence modes of both FW-MAVs are predominantly identified by the sideward transition (δv^+) and the rolling rotation (δp^+), as shown in Figs. 11c1 and c2. The magnitudes of disturbance terms become zero after 10 wingbeats for the SPC (0.43 s), while

they are about 20 wingbeats (0.67 s) for the TEC. This indicates that the convergence speed for the slow subsidence mode of the SPC is about 36% faster than that of the TEC. Fig. 9b shows that the larger magnitude of L_v^+ (positive) induces more instability for the divergence mode, but it is beneficial for the slow subsidence mode. Therefore, in Table 3b, the larger L_v^+ for the SPC, compared to that of the TEC, stabilizes the slow subsidence mode more quickly than for the case of the TEC. Meanwhile, the smaller magnitudes of the damping derivative Y_v^+ and L_p^+ for the SPC may reduce the convergence speed in the slow subsidence mode, as shown in Figs. 9a and h. However, their effects are less significant, compared to that of the L_v^+. Therefore, the larger L_v^+ of the SPC not only contributes to stabilizing the slow subsidence mode, but also disturbs the convergence oscillation mode. Overall, modifying the stroke plane angle of the SPC results in quicker responses comparing with the responses created by adjusting the locations of the trailing edges of the wing roots in the TEC. The quicker responses are beneficial to perform agile maneuverability within a limited space with obstacles. Therefore, the SPC mechanism may be more suitable for tailless insect-like FW-MAVs.

4. Conclusion

In this work, we compared the longitudinal and lateral stability characteristics of the two hovering insect-like tailless FW-MAVs (SPC and TEC). The study indicated that although the system parameters, wing area, and body mass were differently specified for the two FW-MAVs, their flight modes were similar, identified as one stable fast subsidence mode, one stable slow subsidence mode, and one unstable divergence oscillation mode in longitudinal and lateral motions. Furthermore, the difference in magnitudes of the derivatives was the main reason for the stability characteristics of the two FW-MAVs to differ. For the longitudinal motion, the larger M_q^+ and Z_w^+ of the SPC were beneficial for the convergence speed of the fast subsidence mode (+35%) and the slow subsidence mode (+22%), respectively, compared to those of the TEC. Meanwhile, with the larger M_u^+, the divergence mode of the SPC was more unstable (+36%). For the lateral motion, the larger damping derivatives of N_r^+ and L_v^+ of the SPC compared to those of TEC improved the convergence speed for the fast subsidence mode (+44%) and the slow subsidence mode (+36%), respectively. However, it was also found that the larger L_v^+ was a main source of the lateral instability of the SPC, making the FW-MAV unstable faster than the TEC (+36%). In conclusion, the time responses of the SPC due to an external disturbance are relatively quicker than those of the TEC. Therefore, use of the SPC mechanism can allow FW-MAVs to make quicker responses and demonstrate more agile flight to avoid obstacles in highly cluttered habitats, compared to the TEC. The data on the stability analysis of tailless FW-MAVs may provide an insight for future FW-MAV development.

Declaration of competing interest

The authors declare that they have no known competing financial interests or personal relationships that could have appeared to influence the work reported in this paper.

Acknowledgement

This research was supported by a grant to the Bio-Mimetic Robot Research Center (UD190018ID), funded by the Defense Acquisition Program Administration and the Agency for Defense Development.

References

[1] D.E. Alexander, Nature's Flyers: Birds, Insects, and the Biomechanics of Flight, The Johns Hopkins University Press, Baltimore, 2002. Chapter 4.
[2] H.V. Phan, H.C. Park, Insect-inspired, tailless, hover-capable flapping-wing robots: recent progress, challenges, and future directions, Prog. Aerosp. Sci. 111 (2019) 100573.
[3] M. Sun, Insect flight dynamics: stability and control, Rev. Mod. Phys. 86 (2) (2014) 615.
[4] S. Sane, The aerodynamics of insect flight, J. Exp. Biol. 206 (23) (2003) 4191–4208.
[5] M.H. Dickinson, F.O. Lehmann, S.P. Sane, Wing rotation and the aerodynamic basis of insect flight, Science 284 (5422) (1999) 1954–1960.
[6] J.V. Caetano, M. Percin, C.C. De Visser, B. Van Oudheusden, G.C.H.E. De Croon, C. de Wagter, B. Remes, M. Mulder, Tethered vs. free flight force determination of the DelFly II flapping wing micro air vehicle, in: 2014 International Conference on Unmanned Aircraft Systems (ICUAS), IEEE, 2014, pp. 942–948.
[7] T.K.L. Au, H.V. Phan, H.C. Park, Comparison of aerodynamic forces and moments calculated by three-dimensional unsteady blade element theory and computational fluid dynamics, J. Bionics Eng. 14 (4) (2017) 746–758.
[8] H.V. Phan, T.K.L. Au, H.C. Park, Clap-and-fling mechanism in a hovering insect-like two-winged flapping-wing micro air vehicle, R. Soc. Open Sci. 3 (12) (2016) 160746.
[9] S. Deng, J. Wang, H. Liu, Experimental study of a bio-inspired flapping wing MAV by means of force and PIV measurements, Aerosp. Sci. Technol. 94 (2019) 105382.
[10] M. Karásek, F.T. Muijres, C. De Wagter, B.D. Remes, G.C. De Croon, A tailless aerial robotic flapper reveals that flies use torque coupling in rapid banked turns, Science 361 (6407) (2018) 1089–1094.
[11] Z. Tu, F. Fei, X. Deng, Untethered flight of an at-scale dual-motor hummingbird robot with bio-inspired decoupled wings, IEEE Robot. Autom. Lett. 5 (3) (2020) 4194–4201.
[12] S. Aurecianus, H.V. Phan, T.S. Kang, H.C. Park, Longitudinal mode model-based controller design for tailless flapping wing robot with loop shaping compensator, Bioinspir. Biomim. 15 (5) (2020) 056004.
[13] B. Etkin, L.D. Reid, Dynamics of Flight: Stability and Control, John Wiley & Sons Inc., New York, 1996.
[14] T. Nakata, H. Liu, Y. Tanaka, N. Nishihashi, X. Wang, A. Sato, Aerodynamics of a bio-inspired flexible flapping-wing micro air vehicle, Bioinspir. Biomim. 6 (4) (2011) 045002.
[15] M. Sun, Y. Xiong, Dynamic flight stability of a hovering bumblebee, J. Exp. Biol. 208 (3) (2005) 447–459.
[16] G.K. Taylor, A.L.R. Thomas, Animal flight dynamics II. Longitudinal stability in flapping flight, J. Exp. Biol. 214 (3) (2002) 351–370.
[17] G.K. Taylor, A.L.R. Thomas, Dynamic flight stability in the desert locust Schistocerca gregaria, J. Exp. Biol. 206 (16) (2003) 2803–2829.
[18] Y. Zhang, M. Sun, Dynamic flight stability of a hovering model insect: lateral motion, Acta Mech. Sin. 26 (2) (2010) 175–190.
[19] J.S. Han, Interaction of the wakes of two flapping wings on control forces and moment, Aerosp. Sci. Technol. (2021) 106794.
[20] F-O. Lehmann, M.H. Dickinson, The control of wing kinematics and flight forces in fruit flies (Drosophila spp.), J. Exp. Biol. 201 (3) (1998) 385–401.
[21] W. Jiang, Z. Chao, Z. Yanlai, Aerodynamic power efficiency comparison of various micro-air-vehicle layouts in hovering flight, AIAA J. 55 (4) (2016) 1265–1278.
[22] G.K. Taylor, Mechanics and aerodynamics of insect flight control, Biol. Rev. 76 (4) (2001) 449–471.
[23] N. Xu, M. Sun, Lateral dynamic flight stability of a model bumblebee in hovering and forward flight, J. Exp. Biol. 319 (2013) 102–115.
[24] T.K.L. Au, H.C. Park, Influence of center of gravity location on flight dynamic stability in a hovering tailless FW-MAV: longitudinal motion, J. Bionics Eng. 16 (1) (2019) 130–144.
[25] T.K.L. Au, H.C. Park, Influence of center of gravity location on flight dynamic stability in a hovering tailless FW-MAV: lateral motion, J. Bionics Eng. 17 (1) (2020) 148–160.
[26] M. Karásek, Robotic hummingbird: Design of a control mechanism for a hovering flapping wing micro air vehicle, Doctoral dissertation, Universite Libre de Bruxelles, Bruxelles, Belgium, 2014.

[27] X. Ke, W. Zhang, J. Shi, W. Chen, The modeling and numerical solution for flapping wing hovering wingbeat dynamics, Aerosp. Sci. Technol. 110 (2021) 106474.
[28] N. Gao, H. Aono, H. Liu, A numerical analysis of dynamic flight stability of hawkmoth hovering, J. Biomech. Sci. Eng. 4 (1) (2009) 105–116.
[29] X. Mou, M. Sun, Dynamic flight stability of a model hoverfly in inclined-stroke-plane hovering, J. Bionics Eng. 9 (3) (2012) 294–303.
[30] B. Cheng, X. Deng, Translational and rotational damping of flapping flight and its dynamics and stability at hovering, IEEE Trans. Robot. 27 (5) (2011) 849–864.
[31] C.T. Orlowski, A.R. Girard, Stability derivatives for a flapping wing MAV in a hover condition using local averaging, in: Proceedings of the 2005, American Control Conference, 2011, pp. 1604–1609.
[32] Z.A. Khan, S.K. Agrawal, Force and moment characterization of flapping wings for micro air vehicle application, in: Proceedings of the 2005, American Control Conference, 2005, pp. 1515–1520.
[33] Q.T. Truong, Q.V. Nguyen, V.T. Truong, H.C. Park, D.Y. Byun, N.S. Goo, A modified blade element theory for estimation of forces generated by a beetle-mimicking flapping wing system, Bioinspir. Biomim. 6 (3) (2011) 036008.
[34] B. Mi, H. Zhan, Review of numerical simulations on aircraft dynamic stability derivatives, Arch. Comput. Methods Eng. (2019) 1–30.
[35] Y. Xiong, M. Sun, Dynamic flight stability of a bumblebee in forward flight, Acta Mech. Sin. 24 (1) (2008) 25–36.
[36] H.V. Phan, T.S. Kang, H.C. Park, Design and stable flight of a 21 g insect-like tailless flapping wing micro air vehicle with angular rates feedback control, Bioinspir. Biomim. 12 (3) (2017) 036006.
[37] H.V. Phan, H.C. Park, Mechanisms of collision recovery in flying beetles and flapping-wing robots, Science 370 (6521) (2020) 1214–1219.
[38] H.V. Phan, S. Aurecianus, T.K.L. Au, T.S. Kang, H.C. Park, Towards the long-endurance flight of an insect-inspired, tailless, two-winged, flapping-wing flying robot, IEEE Robot. Autom. Lett. 5 (4) (2020) 5059–5066.
[39] H.V. Phan, S. Aurecianus, T.S. Kang, H.C. Park, Attitude control mechanism in an insect-like tailless two-winged flying robot by simultaneous modulation of stroke plane and wing twist, in: International Micro Air Vehicle Conference and Competition, 2018.
[40] T.L. Hedrick, Software techniques for two-and three-dimensional kinematic measurements of biological and biomimetic systems, Bioinspir. Biomim. 3 (3) (2008) 034001.
[41] K. Nguyen, T.K.L. Au, H.V. Phan, S.H. Park, H.C. Park, Effects of wing kinematics, corrugation, and clap-and-fling on aerodynamic efficiency of a hovering insect-inspired flapping-wing micro air vehicle, Aerosp. Sci. Technol. 118 (2021) 106990.
[42] J. Young, J.C. Lai, C. Germain, Simulation and parameter variation of flapping-wing motion based on dragonfly hovering, AIAA J. 46 (4) (2008) 918–924.
[43] Y. Lian, W. Shyy, Aerodynamics of low Reynolds number plunging airfoil under gusty environment, in: The 45th AIAA Aeros. Sci. Meeting and Exhibit, 2007, p. 71.
[44] J.K. Kim, J.S. Han, J.S. Lee, J.H. Han, Hovering and forward flight of the hawkmoth Manduca sexta: trim search and 6-DOF dynamic stability characterization, Bioinspir. Biomim. 10 (5) (2015) 056012.